ACS APPLIED NANO MATERIALS

www.acsanm.org Article

Ultraviolet Photodetectors Based on Nanometer-Thick Films of the Narrow Band Gap Semiconductor PbS

Yue Wang, Di-Hua Lin, Sheng-Hui Luo, Xiang Zhang,* Can Fu, Jiang Wang, Chun-Yan Wu, Di Wu, Yu-Xue Zhou, and Lin-Bao Luo*

Cite This: *ACS Appl. Nano Mater.* 2022, 5, 8894−8901 Read Online

ACCESS | Metrics & More | Article Recommendations | Supporting Information

ABSTRACT: Ultraviolet photodetectors (UVPDs) which play important roles in military and civil applications are normally fabricated by using wide band gap semiconductors (WBSs) as building blocks. Unfortunately, the commercialization of UVPDs based on WBSs is often limited by their relatively high fabrication cost owing to the use of very complicated growth instruments. In this work, a sensitive UVPD based on non-WBS lead sulfide (PbS) with a relatively small band gap was proposed. Device analysis revealed that the UVPD made of 48.5 nm PbS nanofilm was highly sensitive to UV illumination at 365 nm. Specifically, the responsivity and specific detectivity under 365 nm illumination were 22.25 A W^{-1} and 4.97 × 10^{12} Jones, respectively, which are comparable to or better than most of the conventional WBS-based UVPDs. The PbS nanofilm-based UVPD also exhibits excellent environmental stability. Experimental results and simulations based on technology computer-aided design software confirmed that the abnormal properties of PbS nanofilms are related to the relatively thin thickness and wavelength-dependent absorption coefficients. These results open up an opportunity for narrow band gap semiconductors to realize low-cost-sensitive UVPDs in future optoelectronic devices and systems.

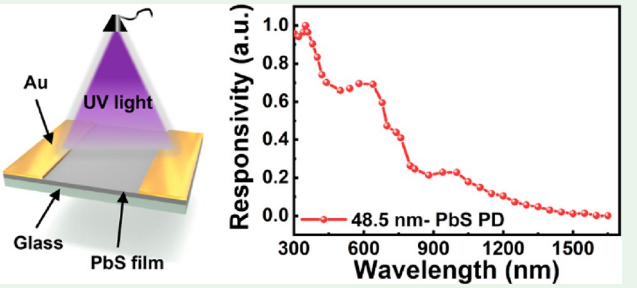

KEYWORDS: *UV photodetector, narrow band gap semiconductor, PbS, high responsivity, technology computer-aided design*

INTRODUCTION

As photoelectronic devices that can accurately change incident light signals into electrical signals, photodetectors (PDs) have attracted much attention in recent years due to their wide applications in multiple detection bands.[1−5] For example, ultraviolet photodetectors (UVPDs) play essential roles in various military and civil applications, such as defense security, UV communication, marine oil pollution monitoring, and health care.[6−9] Normally, wide band gap semiconductors (WBSs, e.g., ZnO, TiO_2, SnO_2, and GaN) are used to fabricate UVPDs.[6,10−13] Based on these WBS-based UVPDs, excellent photoelectric performances in terms of high responsivity, ultralow UV detection limit, and satisfactory stability have been achieved.[14−16] In spite of this, these inorganic WBSs are normally fabricated by using some sophisticated growth instruments,[13,17,18] like metal−organic vapor-phase epitaxy[13] and molecular beam epitaxy,[18] which significantly increased the fabrication costs. While some WBSs (e.g., ZnO and TiO_2) can be synthesized by using the low-cost solution method, the performances of the corresponding PDs are not satisfactory.[19,20] Hence, the low-cost and sensitive UVPDs should be further studied.

In addition to the above conventional WBSs, narrow band gap semiconductors have also been demonstrated to be potential photosensitive materials for the assembly of UVPDs.[21−23] From the perspective of material fabrication and optoelectronic properties, lead sulfide (PbS) shows outstanding advantages, including low cost, mature process, high optical absorption coefficient, and high carrier mobility.[24,25] Due to the narrow band gap of 0.41 eV, the bulk PbS-based PDs are sensitive to infrared (IR) light than UV light.[26−29] However, recent studies have shown that PbS nanocrystals exhibit photoelectric properties different from that of bulk PbS, such as broad spectral response from UV to near-infrared (NIR) and adjustable spectral selectivity.[30−34] Then, the blue shift of the spectral response peak of PbS could be achieved, indicating that it could be used for low-cost and sensitive UVPDs.[35,36]

Inspired by the above works, we here demonstrated a sensitive PbS nanofilm-based UVPD by chemical bath deposition (CBD) method. The proposed UVPD based on narrow band gap nanofilm exhibits good responsivity, high specific detectivity, and excellent environmental stability under

Received: March 10, 2022
Accepted: June 20, 2022
Published: June 28, 2022

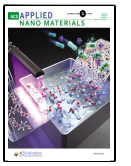

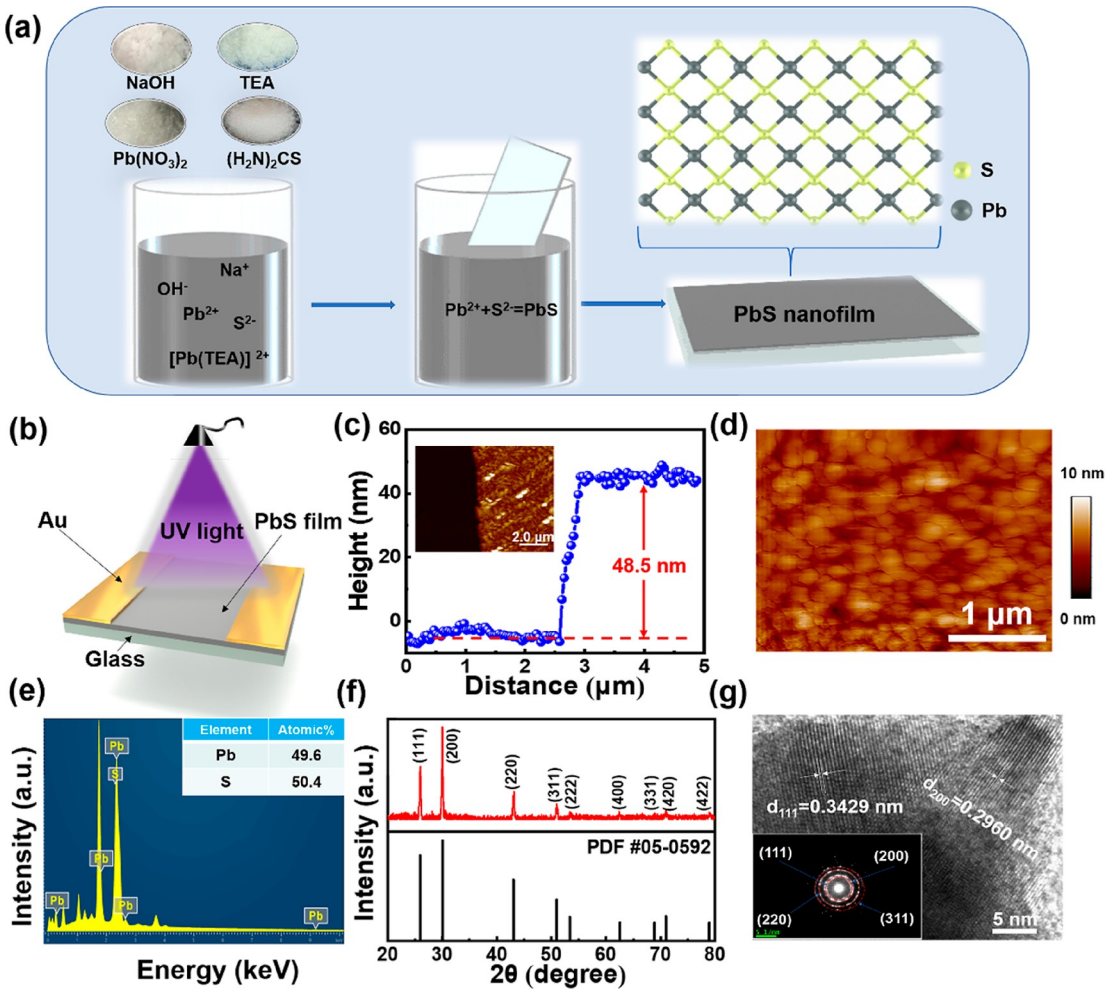

Figure 1. (a) Schematic illustration of the synthesis of a PbS nanofilm by CBD. (b) Schematic illustration of the PbS nanofilm photodetector. (c) Height profile of the PbS nanofilm and AFM image (inset). (d) Two-dimensional AFM image, (e) EDS pattern, and (f) XRD pattern of the PbS nanofilm. (g) HRTEM image of the PbS nanofilm and the corresponding SAED pattern (inset).

365 nm UV irradiation, which are comparable to those of UVPDs based on traditional WBSs. Both experimental and theoretical results revealed that the abnormal properties of the PbS nanofilm are related to the tailoring of the thickness and absorption coefficient. In light of this, we believe our work will open up an opportunity for the development of other low-cost sensitive UVPDs using narrow band gap semiconductors.

EXPERIMENTAL SECTION

Materials Synthesis and Device Fabrication. First, PbS precursor solution was prepared by sequentially mixing 5 mL of 1 mol/L lead nitrate [$(Pb(NO_3)_2)$], 20 mL of 1 mol/L sodium hydroxide (NaOH), 6 mL of 1 mol/L thiourea [$(H_2N)_2CS$], 4 mL of 1 mol/L triethanolamine [$(HOCH_2CH_2)_3N$, TEA], and 65 mL of deionized water. Next, the PbS precursor solution was preheated at 55 °C for 1 min until complete dissolution. Then, acetone, ethanol and deionized water were used sequentially to clean the glass substrates by the ultrasonic bath method for 10−15 min each. After drying for 10 min, the substrates were leaned against a glass beaker. The fabrication conditions (e.g., solution temperature, pH value, and deposition time) were optimized to get repeatable and high-quality PbS nanofilms. Then, PbS nanofilms with different thicknesses (~48.5, ~192, and ~513 nm) were deposited on the glass substrate, respectively, after different deposition durations (~1.5, ~5.5, or ~22 h). Finally, the substrates were rinsed with deionized water to remove surface contaminants.

To fabricate the PbS nanofilm-based photodetectors, the glass substrates with PbS nanofilms were cut into small pieces and transferred into the electron beam evaporator. Au electrodes (50 nm) were deposited on the PbS nanofilm layer by using a laboratory-built metal shadow mask. The channel width (W) of the PDs was about 100 μm.

Material Characterization and Device Analysis. The morphologies and structures of the solution-processed PbS nanofilms were characterized by atomic force microscopy (AFM, Dimension Icon), high-resolution transmission electron microscopy (HRTEM, JEM-2100F), and X-ray diffraction (XRD, PANalytical X-Pert PRO MPD). The absorption spectrum of the PbS nanofilms was measured by a UV−vis−NIR spectrophotometer. The carrier mobility of PbS nanofilms was measured by a ET9000 electrical transport property (Hall effect) measurement system. The photoelectric performances of the PDs were tested by a semiconductor characterization system (4200-SCS, Keithley), and the spectral responses were obtained by a monochromator (LE-SP-M300). Laser diodes with different wavelengths (Thorlabs, 365, 450, 530, 660, 730, 810, 970, 1050, 1300, 1550, and 1650 nm) were used as illumination sources, and their light intensities were calibrated with a power meter (Thorlabs GmbH, PM 100D). All PDs were measured at room temperature.

Theoretical Simulation. Technology computer-aided design (TCAD) software was chosen to simulate the optoelectronic properties of PbS films. In the ATLAS device simulation module, the structure of the device was first constructed in a 2D simulation module. The angle and intensity of incident light were defined so that

https://doi.org/10.1021/acsanm.2c01059
ACS Appl. Nano Mater. 2022, 5, 8894−8901

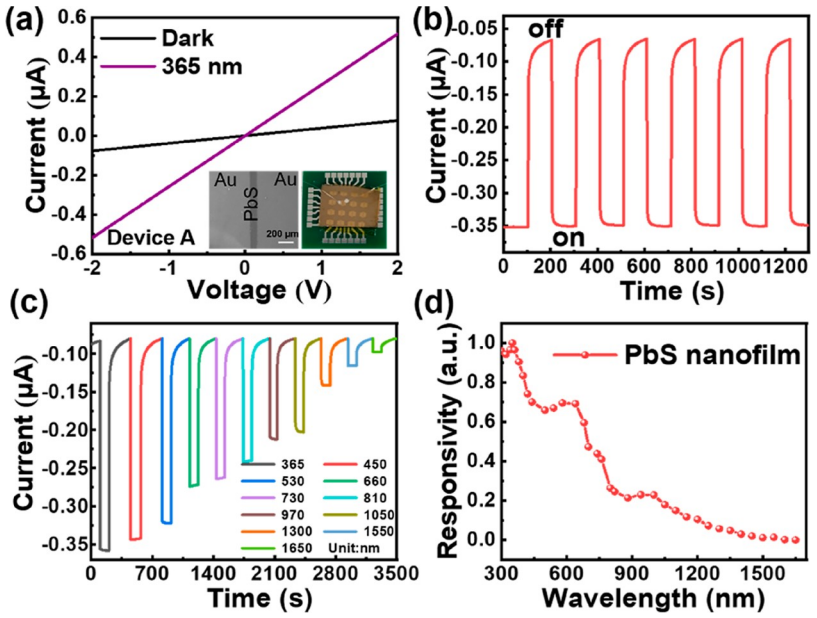

Figure 2. (a) $I-V$ curves of device A in the dark and upon 365 nm illumination. Insets show the corresponding SEM image and camera picture. (b) Switchable photoresponse of device A upon 365 nm light illumination (light intensity: 1.0 mW cm^{-2}) at −2 V bias. (c) Photoresponse curves of device A upon illumination with varied wavelengths. (d) Spectral response of device A at 300−1650 nm wavelength.

the simulated photon absorbance of the device can be obtained. Based on the simulation results, the spectra of the photon absorption rate with different colors were plotted by using the Tonyplot module.

RESULTS AND DISCUSSION

Figure 1a shows the schematic illustration of the procedure for synthesizing a PbS nanofilm. The details of material synthesis are described in Experimental Section and Supporting Information. Here, the PbS nanofilm was synthesized by the CBD method, by which the thickness of the nanofilm can be adjusted by choosing different deposition durations.[37,38] In addition to the ease with thickness control, this solution growth method can avoid the use of sophisticated and expensive instruments, leading to relatively low fabrication costs. The schematic illustration of the PbS nanofilm-based UVPDs is presented in Figure 1b, and the details of the channel length and width are displayed in Figure S1. Figure 1c displays the height profile of the PbS nanofilm along with the AFM image in the inset, from which the film thickness with a deposition time of ∼1.5 h is estimated to be ∼48.5 nm. From further analysis of the film surface roughness in Figures 1d and S2, the arithmetic mean roughness (R_a) and root-mean-square roughness (R_q) are estimated to be 0.712 and 0.914 nm, respectively, which indicate that the continuous PbS nanofilm was obtained. The energy-dispersive spectroscopy (EDS) analysis shows that the elemental ratio (Pb/S) is determined to be 49.6:50.4% [Figure 1e], consistent with the stoichiometric ratio of PbS. Notably, both Pb and S atoms are uniformly distributed on the whole PbS nanofilm, as shown in Figure S3. The XRD pattern of PbS nanofilm is exhibited in Figure 1f. The sharp diffraction peaks indicate that PbS has a high crystalline quality. The representative XRD signals at 25.9, 30.0, 42.9, and 50.9° can be easily attributed to the (111), (200), (220), and (311) planes of PbS [PDF #05-0592].[39] To further study the microstructure of the PbS nanofilm, the HRTEM image and selected area electron diffraction (SAED) pattern were recorded in Figure 1g. It can be seen that the lattice spacing values are about 0.3429 and 0.2960 nm, which correspond to the (111) and (200) lattice planes of the PbS crystal, respectively. In addition, the inset of the SAED pattern also confirms the polycrystalline structure of the PbS nanofilm.

To study the optoelectrical property of the PbS nanofilm, a photodetector based on 48.5 nm PbS nanofilm, as shown in the insets of Figure 2a was prepared and marked as device A. Figure 2a depicts the current−voltage ($I-V$) curves of device A under the dark and 365 nm illumination. The observed linear curve of currents indicates that Ohmic contact was obtained between the gold electrode and the PbS nanofilm. Furthermore, the dark current is −0.077 μA at −2 V. Once shined by 365 nm illumination at 2.5 mW cm^{-2} intensity, the photocurrent significantly increased to −0.517 μA, which means device A is sensitive to UV light illumination. Then, the switching characteristics of device A were investigated under periodically switchable UV irradiation. As shown in Figure 2b, at a bias of −2 V with 365 nm illumination (light intensity, 1.0 mW cm^{-2}), the dark current and photocurrent are −0.077 and −0.35 μA, respectively. Besides the sensitivity to UV light, device A also exhibits a relatively weak photoresponse to long-wavelength light (visible and NIR), as shown in Figure 2c. To further confirm the above conclusion, the spectral response was recorded in Figure 2d under the illumination with 300−1650 nm wavelength range. It can be seen that the device A exhibits a broad spectral response. More importantly, the photoresponse peak of device A is located in the UV region, which is quite different from that of previously reported PbS-based PDs, including PbS quantum dot-based PDs,[40,41] PbS nanoplate array-based PDs,[24] PbS nanocrystal-based PDs,[30] and commercial bulk PbS-based PDs.[42] It is worth to notice that the detection of UV light may be affected by visible light for device A, which is similar to some conventional WBS-based PDs.[43−45] However, the UV-to-visible rejection ratio can be further improved by adjusting the thickness of the PbS nanofilm or utilizing resonant field enhancement strategies.[22,46]

Further device analysis found that the photoresponse is strongly dependent on the incident UV illumination intensity.

https://doi.org/10.1021/acsanm.2c01059
ACS Appl. Nano Mater. 2022, 5, 8894−8901

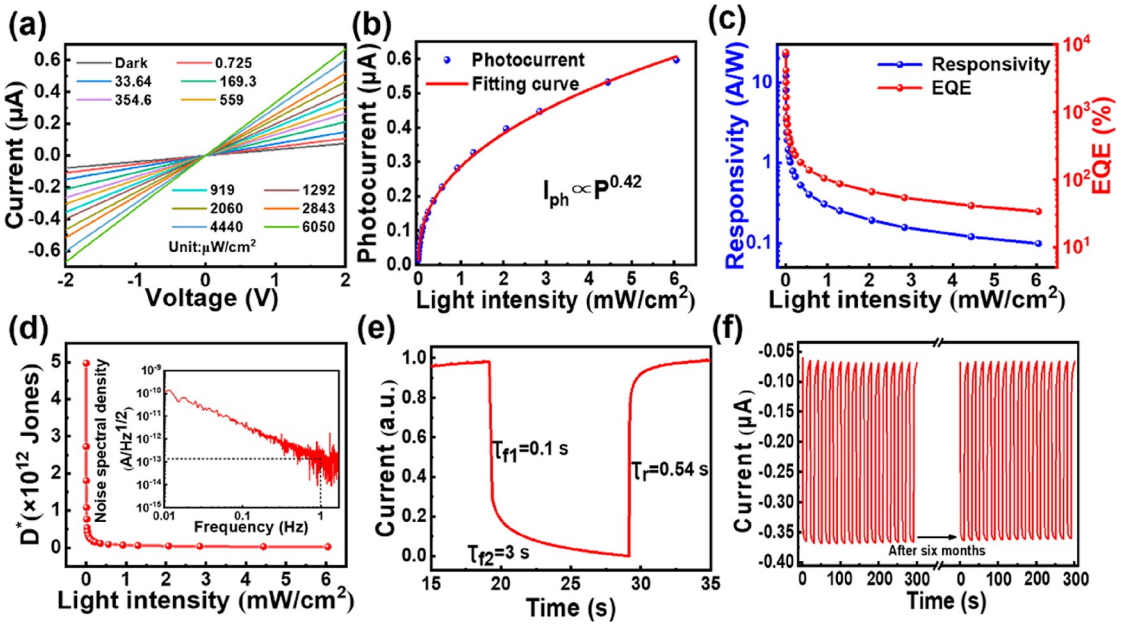

Figure 3. (a) $I-V$ curves of device A upon 365 nm illumination with different light intensities. (b) Photocurrent, (c) R, and EQE of device A as functions of light intensity at −2 V bias. (d) D^* of device A at various light intensities. The inset shows the noise spectral density of device A based on the Fourier transform of the dark current. (e) One cycle of the photoresponse of device A for determining the rise and fall times. (f) Comparison of time-dependent photoresponse for about 15 cycles before and after 6 months' air storage.

Table 1. Comparison of Some Representative Parameters of Device A and Other UVPDs Composed of Traditional WBSs

materials	wavelength (nm)	dark current (A)	R [A W^{-1}]	D^* (Jones)	τ_r/τ_f (s)	refs
ZnO	370	3.61×10^{-9}	12		250/150	10
TiO_2	312	1.1×10^{-9}	13		0.5/0.7	48
MgZnO	350		5.91×10^{-4}	2.7×10^{6}	30.9/39.7	49
$CH_3NH_3PbCl_3$	365	4.15×10^{-7}	4.69×10^{-2}	1.2×10^{10}	0.024/0.062	50
SiC	365	2×10^{-6}	55.89	1.22×10^{8}	4/2.5	51
a-GaN	364		400	6.6×10^{12}	0.173/1.21	52
PbS nanofilm	365	7.7×10^{-8}	22.25	4.97×10^{12}	0.54/(0.1/3)	this work

Figure 3a presents the $I-V$ curves of device A under 365 nm illumination with different light intensities. Notably, the current increases monotonically with the increase of light intensity. Similar results were also found from the current−time ($I-T$) curves of device A shown in Figure S4. This is caused by the increase of photogenerated carriers under higher intensity UV irradiation. The relationship between photocurrent and power intensity can be numerically fitted by $I_{ph} \propto P^{\theta}$ ($\theta = 0.42$), as shown in Figure 3b, where I_{ph} denotes the net photocurrent and P denotes the power intensity. The exponent θ is a fitting value related to the recombination loss, which may arise from the photocarriers' recombination in the PbS nanofilm. In addition, we investigated the linear dynamic range (LDR) of the device by the formula: LDR = 20 log (I_{ph}/I_d), where I_{ph} denotes the photocurrent (0.338 μA) and I_d denotes the dark current (0.077 μA), respectively. As shown in Figure S5, the LDR of device A was 12.84 dB. To evaluate the photoresponse performance of device A, key performance parameters, including responsivity (R), external quantum efficiency (EQE), and specific detectivity (D^*), are calculated by the following equations

$$R = \frac{I_{ph}}{SP} \tag{1}$$

$$\mathrm{EQE} = \frac{hcR}{e\lambda} \tag{2}$$

$$D^* = \frac{R(S\Delta f)^{1/2}}{\overline{i_n^2}^{1/2}} \tag{3}$$

where I_{ph} is the net photocurrent, S is the effective device area (1.0×10^{-3} cm^2), P is the incident light intensity, h, c, e, λ, and Δ represent the Planck constant, light speed, elementary electrical charge, incident light wavelength, and specific bandwidth, respectively. $\overline{i_n^2}^{1/2}$ denotes the root-mean-square value of the noise current. As illustrated in Figure 3c, both R and EQE will decline when the light intensity increases, which confirms the photocarriers' recombination loss when illuminated by a relatively strong UV light. The maximum R and EQE of device A are 22.25 A W^{-1} and 7.573×10^3% under 365 nm illumination, respectively. Moreover, a high gain (G) of 75.73 at a −2 V bias can be achieved by calculating with the equation of $G = hcR/\eta e\lambda$, where η means internal quantum efficiency. The high gain here is mainly caused by the applied voltage and the trap state on the surface of the film.[47] From the inset of Figure 3d, the noise spectral density of device A is estimated to be 1.42×10^{-13} A Hz$^{-1/2}$ at 1 Hz. A similar phenomenon was also found for D^*, and the highest D^* was calculated to be 4.97×10^{12} Jones. From the single $I-T$ curve

https://doi.org/10.1021/acsanm.2c01059
ACS Appl. Nano Mater. 2022, 5, 8894−8901

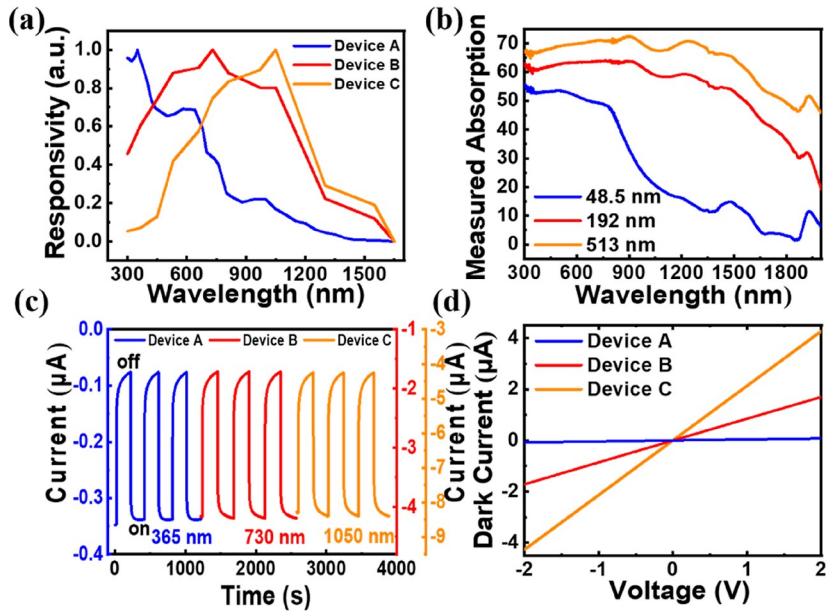

Figure 4. (a) Normalized spectral responsivity of PbS nanofilms with different thicknesses. (b) Experimental absorption curves of PbS nanofilms with different thicknesses. (c) Photoresponse of PbS nanofilms of different thicknesses at peak wavelength with a light intensity of 1.0 mW cm^{-2} at −2 V. (d) Dark current of PbS nanofilms with different thicknesses.

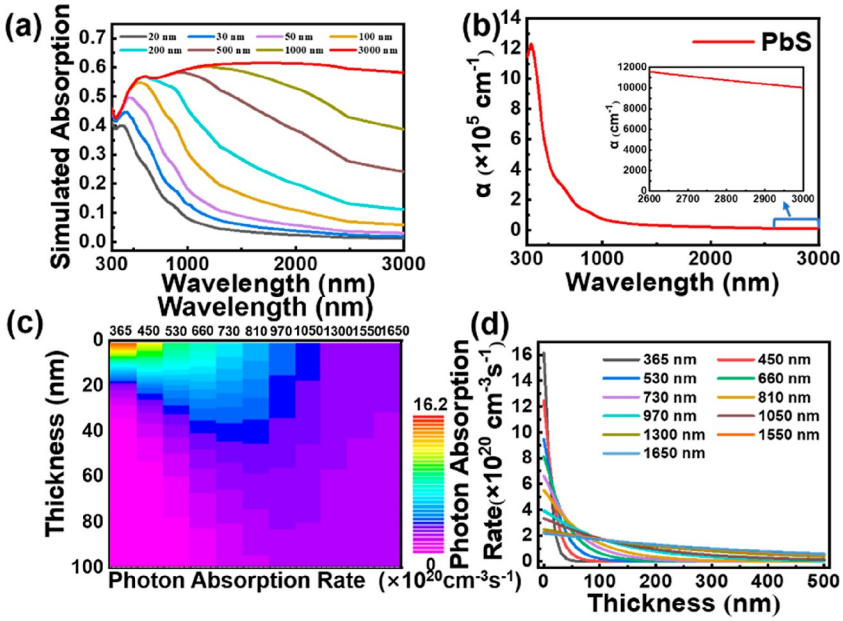

Figure 5. (a) Simulated absorption curves of PbS films with thicknesses of 20−3000 nm at wavelengths of 300−3000 nm. (b) Absorption coefficient of the PbS film. (c) Simulated photon absorption rate under wavelengths of 365−1650 nm for PbS devices. (d) Photon absorption rate curves of PbS films under 365−1650 nm.

magnified in Figure 3e, the rise time (τ_r) and fall time (τ_{f1} and τ_{f2}) are calculated to be about 0.54 s and 0.1/3 s, respectively. Furthermore, device A also exhibits excellent ambient stability, as shown in Figures 3f and S6. Even after the storage in an air environment without any protection for 6 months or thousands of cycles of operation under UV illumination, the photocurrent of device A did not show any degradation, which is probably due to the good stability of the PbS nanofilm. Table 1 compares some representative parameters (dark current, R, D^*, and τ_r/τ_{f1}, τ_{f2}) of device A and other UVPDs composed of traditional WBSs.[10,48−52] However, the dark current and rise/fall time of device A did not show obvious advantages in comparison with these WBS-based UVPDs. Nevertheless, the R and D^* values of device A are superior to those of most other WBS-based UVPDs consisting of ZnO, TiO_2, MgZnO, and $CH_3NH_3PbCl_3$.[10,48−50]

By comparing the performances of PDs with PbS nanofilms of different thicknesses, the reason why device A is more sensitive to UV light than visible and NIR light has been investigated. For the sake of convenience, other devices made of PbS nanofilms with thicknesses of ∼192 nm (device B) and ∼513 nm (device C) have been assembled as well, as shown in Figure S7a,b. Figure 4a depicts the normalized spectral response of devices A−C. It can be found that the response

https://doi.org/10.1021/acsanm.2c01059
ACS Appl. Nano Mater. 2022, 5, 8894−8901

peak is found to significantly blue-shift with decreasing thickness (device A: peak in the UV region; device B: peak in the visible light region; device C: peak in the NIR region). Note that the carrier mobilities of devices A−C were measured by the Hall effect (device A: 1.89679×10^2 cm^2 v^{-1} s^{-1}; device B: 1.65158×10^2 cm^2 v^{-1} s^{-1}; and device C: 1.79725×10^2 cm^2 v^{-1} s^{-1}), which are better than the previously reported results.[53] Then, the drift length was calculated to be ∼380 μm,[54,55] which means that the photogenerated carriers in devices A−C can drift to the electrodes to generate photocurrent. Thus, such a thickness-dependent spectral response is consistent with the optical property. The absolute light absorption intensity decreases with the decrease of PbS nanofilm thickness, as shown in Figure 4b. Moreover, the absorption in the visible and IR bands decreases obviously for the 48.5 nm PbS nanofilm, leading to the relatively strong absorption in the UV band. Such an abnormal phenomenon is interesting and renders the present PbS nanofilm a potential candidate for UVPD application in that the optical absorption and the resultant photoelectric property can be easily adjusted by its thickness. Furthermore, by irradiating each device at their respective response peak wavelengths, the photoresponses of devices A−C were measured, as shown in Figure 4c. It is clear that all three devices exhibit excellent switching characteristics and reproducibility at their respective peak responses, while their photocurrents are completely different: device A has a typical photocurrent of only −0.35 μA under 365 nm illumination. As the thickness of the PbS nanofilm gradually increases to 192 and 513 nm, the corresponding devices (devices B and C) display increased photocurrent with increasing thickness. This finding can be explained by the reduced light absorption region and the collection number of photogenerated carriers.[56] Furthermore, the increased conductivity of the PbS nanofilm is also a contributory factor. As a way to describe the conductivity of the semiconductor films, the sheet resistance (R_s) is calculated as $R_s = (\text{rho} \times L)/(t \times W)$, where rho is the resistivity, and L, W, and t are the length, width, and thickness of the semiconductor material, respectively. The resistivities of the three devices are approximately the same due to the similar carrier mobility. Further, L and W are the same for the three devices. Then, the sheet resistances of our devices decrease with the increase of the thickness, and the corresponding results can be seen from the dark currents of the three devices in Figure 4d.

To further unveil the reason for the observed UV sensitivity at the PbS nanofilm, the photoabsorption and photon absorption rates of PbS films were simulated by using TCAD software. First, the simulated photoabsorption curves of PbS films with different thicknesses are plotted in Figure 5a. Obviously, with the decrease of thickness, the absorption intensity of long-wavelength light (visible and IR) decreases significantly, and absorption with a relatively high intensity shifts to the UV region, which means the PbS nanofilms exhibit completely different optical properties from bulk PbS. Such a thickness-dependent optical property of PbS nanofilms can be explained by the wavelength-dependent absorption coefficient (α). Figure 5b plots the variation of α with wavelength. It can be found that α of the PbS film decreases substantially with the increase of wavelength. Specifically, α corresponding to 320 nm is 1.185×10^6 cm^{-1}, which is about 2 orders of magnitude higher than α at 2400 nm. This huge difference leads to completely different penetration depths (the physical thickness at which incident light can penetrate into the semiconductor material) for various wavelengths. Note that the value of absorption coefficient is still high at ∼3000 nm wavelength [the insert of Figure 5b]. Then, lots of photons at the wavelength of ∼3000 nm will be absorbed in 3000 nm thick PbS film, leading to a high absorbance. Figure 5c shows the spatial distribution of the photon absorption rate of PbS at wavelengths from 365 to 1650 nm. It can be seen that most of the photon absorption takes place on the surface of the PbS film under short-wavelength irradiation. However, the photon absorption of PbS nanofilm moves to a deep area of PbS film with the increase of wavelength. Therefore, reducing the thickness of the PbS film reduces the absorption of relatively longer wavelengths of light, rendering thinner PbS films very sensitive to UV light.[22,57] Moreover, it can be speculated that it is possible to achieve deep ultraviolet PD by using ultrathin nanofilms. The above optical properties of the PbS film can be further verified from Figure 5d, which plots the numerical profiles of photon absorption rate of the PbS film under light irradiation from 365 to 1650 nm. The maximum photon absorption rate under 365 nm illumination is 1.62×10^{21} cm^{-3} s^{-1} at the superficial surface of the PbS film, suggesting that the absorption of thinner PbS film is dominated by UV light.[58] This result, which is in sharp contrast with the case when irradiated by NIR illumination, confirms that sensitive UVPDs can be realized by tailoring the thickness of the narrow band gap semiconductor nanofilm.

CONCLUSIONS

In summary, a highly sensitive UVPD was reported by using a non-WBS PbS nanofilm with a thickness of 48.5 nm. The PbS PD was sensitive to 365 nm UV illumination with a responsivity of 22.25 A W^{-1} and a specific detectivity of 4.97×10^{12} Jones, which is comparable or even better than other UVPDs made of WBS material. Besides, PbS nanofilm-based UVPD also exhibits good environmental stability. Simulation results based on TCAD reveal that this abnormal photoresponse of the narrow band gap semiconductor to UV light illumination is associated with the thin thickness and absorption coefficient of the PbS film. These results open up an opportunity for narrow band gap semiconductors to realize sensitive UVPDs in future optoelectronic devices and systems.

ASSOCIATED CONTENT

Supporting Information

The Supporting Information is available free of charge at https://pubs.acs.org/doi/10.1021/acsanm.2c01059.

Device scheme with full geometry of the channel; three-dimensional AFM image of the PbS nanofilm; elemental mapping results of both Pb and S elements; photoresponse of device A upon 365 nm illumination with different light intensities at −2 V bias; fitting of the curve of photocurrent versus light intensity; photoresponse of device A over thousands of cycles of operation under the UV environment; and height profiles of PbS nanofilms with the thickness of 192 nm and 513 nm, the insets showing the corresponding AFM images and camera pictures (PDF)

https://doi.org/10.1021/acsanm.2c01059
ACS Appl. Nano Mater. 2022, 5, 8894−8901

AUTHOR INFORMATION

Corresponding Authors

Xiang Zhang − *School of Microelectronics, Hefei University of Technology, Hefei 230009, China;* orcid.org/0000-0001-7002-6706; Email: zhangx@hfut.edu.cn

Lin-Bao Luo − *School of Microelectronics, Hefei University of Technology, Hefei 230009, China;* orcid.org/0000-0001-8651-8764; Email: luolb@hfut.edu.cn

Authors

Yue Wang − *School of Microelectronics, Hefei University of Technology, Hefei 230009, China*

Di-Hua Lin − *School of Physics, Hefei University of Technology, Hefei 230009, China*

Sheng-Hui Luo − *School of Microelectronics, Hefei University of Technology, Hefei 230009, China*

Can Fu − *School of Microelectronics, Hefei University of Technology, Hefei 230009, China*

Jiang Wang − *School of Microelectronics, Hefei University of Technology, Hefei 230009, China*

Chun-Yan Wu − *School of Microelectronics, Hefei University of Technology, Hefei 230009, China;* orcid.org/0000-0001-5793-6772

Di Wu − *Key Laboratory of Materials Physics of Ministry of Education, Department of Physics and Engineering, Zhengzhou University, Zhengzhou 450052, China;* orcid.org/0000-0003-3266-0612

Yu-Xue Zhou − *College of Physical Science and Technology, Yangzhou University, Yangzhou 225002, China*

Complete contact information is available at: https://pubs.acs.org/10.1021/acsanm.2c01059

Author Contributions

Y.W. and D.-H.L. synthesized the samples, prepared the device, and analyzed the device performance. L.-B.L. and X.Z. conceived these experiments. C.F. simulated the device. C.-Y.W., Y.-X.Z., and D.W. contributed to the study of optical properties and physical mechanisms of materials. J.W. and S.-H.L. helped with the synthesis of the materials and characterization. The manuscript is written by Y.W. and discussed by all authors.

Notes

The authors declare no competing financial interest.

ACKNOWLEDGMENTS

This work was supported by the National Natural Science Foundation of China (NSFC, nos. 62074048), the Fundamental Research Funds for the Central Universities (JZ2018HGXC0001), and the Open Foundation of Anhui Provincial Key Laboratory of Advanced Functional Materials and Devices (4500-411104/011).

REFERENCES

(1) Koppens, F. H. L.; Mueller, T.; Avouris, P.; Ferrari, A. C.; Vitiello, M. S.; Polini, M. Photodetectors based on graphene, other two-dimensional materials and hybrid systems. *Nat. Nanotechnol.* **2014**, *9*, 780−793.

(2) Chen, H.; Liu, H.; Zhang, Z.; Hu, K.; Fang, X. Nanostructured Photodetectors: From Ultraviolet to Terahertz. *Adv. Mater.* **2016**, *28*, 403−433.

(3) Teng, F.; Hu, K.; Ouyang, W.; Fang, X. Photoelectric Detectors Based on Inorganic p-Type Semiconductor Materials. *Adv. Mater.* **2018**, *30*, 1706262.

(4) Wu, W.; Wang, X.; Han, X.; Yang, Z.; Gao, G.; Zhang, Y.; Hu, J.; Tan, Y.; Pan, A.; Pan, C. Flexible Photodetector Arrays Based on Patterned $CH_3NH_3PbI_{3-x}Cl_x$ Perovskite Film for Real-Time Photosensing and Imaging. *Adv. Mater.* **2019**, *31*, 1805913.

(5) Li, Z.; Xu, K.; Wei, F. Recent progress in photodetectors based on low-dimensional nanomaterials. *Nanotechnol. Rev.* **2018**, *7*, 393−411.

(6) Qiu, M.; Sun, P.; Liu, Y.; Huang, Q.; Zhao, C.; Li, Z.; Mai, W. Visualized UV Photodetectors Based on Prussian Blue/TiO_2 for Smart Irradiation Monitoring Application. *Adv. Mater. Technol.* **2018**, *3*, 1700288.

(7) Goossens, S.; Navickaite, G.; Monasterio, C.; Gupta, S.; Piqueras, J. J.; Pérez, R.; Burwell, G.; Nikitskiy, I.; Lasanta, T.; Galán, T.; Puma, E.; Centeno, A.; Pesquera, A.; Zurutuza, A.; Konstantatos, G.; Koppens, F. Broadband image sensor array based on graphene−CMOS integration. *Nat. Photonics* **2017**, *11*, 366−371.

(8) Wu, D.; Hu, Q.; Yan, Z.; Chen, W.; Yan, C.; Huang, X.; Zhang, J.; Yang, P.; Deng, H.; Wang, J.; Deng, X.; Shi, Y. Structural basis of ultraviolet-B perception by UVR8. *Nature* **2012**, *484*, 214−219.

(9) Premi, S.; Wallisch, S.; Mano, C. M.; Weiner, A. B.; Bacchiocchi, A.; Wakamatsu, K.; Bechara, E. J. H.; Halaban, R.; Douki, T.; Brash, D. E. Chemiexcitation ofmelanin derivatives induces DNA photoproducts long after UV exposure. *Science* **2015**, *347*, 842−847.

(10) Nasiri, N.; Bo, R.; Wang, F.; Fu, L.; Tricoli, A. Ultraporous Electron-Depleted ZnO Nanoparticle Networks for Highly Sensitive Portable Visible-Blind UV Photodetectors. *Adv. Mater.* **2015**, *27*, 4336−4343.

(11) Jin, Z.; Zhou, Q.; Chen, Y.; Mao, P.; Li, H.; Liu, H.; Wang, J.; Li, Y. Graphdiyne:ZnO Nanocomposites for High-Performance UV Photodetectors. *Adv. Mater.* **2016**, *28*, 3697−3702.

(12) Liu, K.; Sakurai, M.; Aono, M.; Shen, D. Ultrahigh-Gain Single SnO_2 Microrod Photoconductor on Flexible Substrate with Fast Recovery Speed. *Adv. Funct. Mater.* **2015**, *25*, 3157−3163.

(13) Cai, Y.; Shen, S.; Zhu, C.; Zhao, X.; Bai, J.; Wang, T. Nonpolar (1120) GaN Metal−Semiconductor−Metal Photodetectors with Superior Performance on Silicon. *ACS Appl. Mater. Interfaces* **2020**, *12*, 25031−25036.

(14) Alaie, Z.; Mohammad Nejad, S.; Yousefi, M. H. Recent advances in ultraviolet photodetectors. *Mater. Sci. Semicond. Process.* **2015**, *29*, 16−55.

(15) Zou, Y.; Zhang, Y.; Hu, Y.; Gu, H. Ultraviolet Detectors Based on Wide Bandgap Semiconductor Nanowire: A Review. *Sensors* **2018**, *18*, 2072.

(16) Zhou, C.; Ai, Q.; Chen, X.; Gao, X.; Liu, K.; Shen, D. Ultraviolet photodetectors based on wide bandgap oxide semiconductor films. *Chin. Phys. B* **2019**, *28*, 048503.

(17) Tan, S. T.; Chen, B. J.; Sun, X. W.; Fan, W. J.; Kwok, H. S.; Zhang, X. H.; Chua, S. J. Blueshift of optical band gap in ZnO thin films grown by metal-organic chemical-vapor deposition. *J. Appl. Phys.* **2005**, *98*, 013505.

(18) Bonef, B.; Cramer, R.; Speck, J. S. Nanometer scale composition study of MBE grown BGaN performed by atom probe tomography. *J. Appl. Phys.* **2017**, *121*, 225701.

(19) Liu, J.; Lu, R.; Xu, G.; Wu, J.; Thapa, P.; Moore, D. Development of a Seedless Floating Growth Process in Solution for Synthesis of Crystalline ZnO Micro/Nanowire Arrays on Graphene: Towards High-Performance Nanohybrid Ultraviolet Photodetectors. *Adv. Funct. Mater.* **2013**, *23*, 4941−4948.

(20) Xue, H.; Kong, X.; Liu, Z.; Liu, C.; Zhou, J.; Chen, W.; Ruan, S.; Xu, Q. TiO_2 based metal-semiconductor-metal ultraviolet photodetectors. *Appl. Phys. Lett.* **2007**, *90*, 201118.

(21) Wang, J.-J.; Fu, C.; Cheng, H.-Y.; Tong, X.-W.; Zhang, Z.-X.; Wu, D.; Chen, L.-M.; Liang, F.-X.; Luo, L.-B. Leaky Mode Resonance-Induced Sensitive Ultraviolet Photodetector Composed of Graphene/Small Diameter Silicon Nanowire Array Heterojunctions. *ACS Nano* **2021**, *15*, 16729−16737.

(22) Ali, A.; Shehzad, K.; Guo, H. W.; Wang, Z.; Wang, P.; Qadir, A.; Hu, W. D.; Ren, T. L.; Yu, B.; Xu, Y. *High-Performance, Flexible Graphene/Ultra-Thin Silicon Ultra-Violet Image Sensor*; IEEE Interna-

tional Electron Devices Meeting (IEDM): San Francisco, CA, USA, December 2−6, 2017; pp 8.6.1−8.6.4.
(23) Cao, R.; Zhang, Y.; Wang, H.; Zeng, Y.; Zhao, J.; Zhang, L.; Li, J.; Meng, F.; Shi, Z.; Fan, D.; Guo, Z. Solar-blind deep-ultraviolet photodetectors based on solution-synthesized quasi-2D Te nanosheets. *Nanophotonics* **2020**, *9*, 2459−2466.
(24) Wen, Y.; Wang, Q.; Yin, L.; Liu, Q.; Wang, F.; Wang, F.; Wang, Z.; Liu, K.; Xu, K.; Huang, Y.; Shifa, T. A.; Jiang, C.; Xiong, J.; He, J. Epitaxial 2D PbS Nanoplates Arrays with Highly Efficient Infrared Response. *Adv. Mater.* **2016**, *28*, 8051−8057.
(25) Li, X.-B.; Guo, P.; Zhang, Y.-N.; Peng, R.-F.; Zhang, H.; Liu, L.-M. High carrier mobility of few-layer PbX (X = S, Se, Te). *J. Mater. Chem. C* **2015**, *3*, 6284−6290.
(26) Xu, K.; Xiao, X.; Zhou, W.; Jiang, X.; Wei, Q.; Chen, H.; Deng, Z.; Huang, J.; Chen, B.; Ning, Z. Inverted Si:PbS Colloidal Quantum Dot Heterojunction-Based Infrared Photodetector. *ACS Appl. Mater. Interfaces* **2020**, *12*, 15414−15421.
(27) Yang, C.; Feng, S.; Tang, L.; Shen, J.; Wei, X.; Shi, H. Electrochemical Epitaxial Grown PbS Nanorods Array on Graphene Film for High-Performance Photodetector. *Adv. Mater. Interfaces* **2020**, *8*, 2001464.
(28) Killilea, N.; Wu, M.; Sytnyk, M.; Yousefi Amin, A. A.; Mashkov, O.; Spiecker, E.; Heiss, W. Pushing PbS/Metal-Halide-Perovskite Core/Epitaxial-Ligand-Shell Nanocrystal Photodetectors beyond 3 μm Wavelength. *Adv. Funct. Mater.* **2019**, *29*, 1807964.
(29) Moss, T. Lead salt photoconductors. *Proc. IRE* **1955**, *43*, 1869−1881.
(30) Lee, J. W.; Kim, D. Y.; Baek, S.; Yu, H.; So, F. Inorganic UV-Visible-SWIR Broadband Photodetector Based on Monodisperse PbS Nanocrystals. *Small* **2016**, *12*, 1328−1333.
(31) Gao, L.; Chen, H.; Wang, R.; Wei, S.; Kuklin, A. V.; Mei, S.; Zhang, F.; Zhang, Y.; Jiang, X.; Luo, Z.; Xu, S.; Zhang, H.; Agren, H. Ultra-Small 2D PbS Nanoplatelets: Liquid-Phase Exfoliation and Emerging Applications for Photo-Electrochemical Photodetectors. *Small* **2021**, *17*, No. e2005913.
(32) Saran, R.; Curry, R. J. Lead sulphide nanocrystal photodetector technologies. *Nat. Photonics* **2016**, *10*, 81−92.
(33) Wang, Y.; Liu, Z.; Huo, N.; Li, F.; Gu, M.; Ling, X.; Zhang, Y.; Lu, K.; Han, L.; Fang, H.; Shulga, A. G.; Xue, Y.; Zhou, S.; Yang, F.; Tang, X.; Zheng, J.; Antonietta Loi, M.; Konstantatos, G.; Ma, W. Room-temperature direct synthesis of semi-conductive PbS nanocrystal inks for optoelectronic applications. *Nat. Commun.* **2019**, *10*, 5136.
(34) Khanzode, P. M.; Halge, D. I.; Narwade, V. N.; Dadge, J. W.; Bogle, K. A. Highly photoresponsive visible light photodetector using nano PbS thin film on paper. *Optik* **2021**, *226*, 165933.
(35) Smith, A.; Dutton, D. Behavior of Lead Sulfide Photocells in the Ultraviolet. *J. Opt. Soc. Am.* **1958**, *48*, 1007−1009.
(36) Dehdashti Jahromi, H.; Moaddeli, M. Lead sulfide; a new candidate for optoelectronics applications in the ultra violet spectral range. *Mater. Res. Express* **2019**, *6*, 116220.
(37) Pawar, S. M.; Pawar, B. S.; Kim, J. H.; Joo, O.-S.; Lokhande, C. D. Recent status of chemical bath deposited metal chalcogenide and metal oxide thin films. *Curr. Appl. Phys.* **2011**, *11*, 117−161.
(38) Tohidi, T.; Jamshidi-Ghaleh, K.; Namdar, A.; Abdi-Ghaleh, R. Comparative studies on the structural, morphological, optical, and electrical properties of nanocrystalline PbS thin films grown by chemical bath deposition using two different bath compositions. *Mater. Sci. Semicond. Process.* **2014**, *25*, 197−206.
(39) Xie, B. H.; Fei, G. T.; Xu, S. H.; Gao, X. D.; Zhang, J. X.; Zhang, L. D. Tunable broadband wavelength-selective enhancement of responsivity in ordered Au-nanorod array-modified PbS photodetectors. *J. Mater. Chem. C* **2018**, *6*, 1767−1773.
(40) Sun, Z.; Liu, Z.; Li, J.; Tai, G.-a.; Lau, S.-P.; Yan, F. Infrared photodetectors based on CVD-grown graphene and PbS quantum dots with ultrahigh responsivity. *Adv. Mater.* **2012**, *24*, 5878−5883.
(41) Ren, Z.; Sun, J.; Li, H.; Mao, P.; Wei, Y.; Zhong, X.; Hu, J.; Yang, S.; Wang, J. Bilayer PbS Quantum Dots for High-Performance Photodetectors. *Adv. Mater.* **2017**, *29*, 1702055.
(42) https://www.thorlabs.com/thorproduct.cfm?partnumber=FDPS3X3 (accessed 01-06-2022).
(43) Yuan, Z.; Wang, W.; Wu, H.; Nie, F.; He, J. A solution-processed ZnO quantum dots ultraviolet photodetector with high performance driven by low operating voltage. *Mater. Lett.* **2020**, *278*, 128413.
(44) Nie, B.; Hu, J.-G.; Luo, L.-B.; Xie, C.; Zeng, L.-H.; Lv, P.; Li, F.-Z.; Jie, J.-S.; Feng, M.; Wu, C.-Y.; Yu, Y.-Q.; Yu, S.-H. Monolayer graphene film on ZnO nanorod array for high-performance Schottky junction ultraviolet photodetectors. *Small* **2013**, *9*, 2872−2879.
(45) Kunwar, S.; Pandit, S.; Kulkarni, R.; Mandavkar, R.; Lin, S.; Li, M.-Y.; Lee, J. Hybrid Device Architecture Using Plasmonic Nanoparticles, Graphene Quantum Dots, and Titanium Dioxide for UV Photodetectors. *ACS Appl. Mater. Interfaces* **2021**, *13*, 3408−3418.
(46) Wang, Q.; Guo, J.; Ding, Z.; Qi, D.; Jiang, J.; Wang, Z.; Chen, W.; Xiang, Y.; Zhang, W.; Wee, A. T. S. Fabry-Perot Cavity-Enhanced Optical Absorption in Ultrasensitive Tunable Photodiodes Based on Hybrid 2D Materials. *Nano Lett.* **2017**, *17*, 7593−7598.
(47) Xie, C.; Lu, X.-T.; Tong, X.-W.; Zhang, Z.-X.; Liang, F.-X.; Liang, L.; Luo, L.-B.; Wu, Y.-C. Recent Progress in Solar-Blind Deep-Ultraviolet Photodetectors Based on Inorganic Ultrawide Bandgap Semiconductors. *Adv. Funct. Mater.* **2019**, *29*, 1806006.
(48) Zou, J.; Zhang, Q.; Huang, K.; Marzari, N. Ultraviolet Photodetectors Based on Anodic TiO_2 Nanotube Arrays. *J. Phys. Chem. C* **2010**, *114*, 10725−10729.
(49) Young, S.-J.; Liu, Y.-H. Low-frequency noise properties of MgZnO nanorod ultraviolet photodetectors with and without UV illumination. *Sens. Actuators, A* **2018**, *269*, 363−368.
(50) Maculan, G.; Sheikh, A. D.; Abdelhady, A. L.; Saidaminov, M. I.; Haque, M. A.; Murali, B.; Alarousu, E.; Mohammed, O. F.; Wu, T.; Bakr, O. M. $CH_3NH_3PbCl_3$ Single Crystals: Inverse Temperature Crystallization and Visible-Blind UV-Photodetector. *J. Phys. Chem. Lett.* **2015**, *6*, 3781−3786.
(51) Liang, S.; Dai, Y.; Wang, G.; Xia, H.; Zhao, J. Room-temperature fabrication of SiC microwire photodetectors on rigid and flexible substrates via femtosecond laser direct writing. *Nanoscale* **2020**, *12*, 23200−23205.
(52) Pant, R.; Singh, D. K.; Chowdhury, A. M.; Roul, B.; Nanda, K. K.; Krupanidhi, S. B. Highly Responsive, Self-Powered a-GaN Based UV-A Photodetectors Driven by Unintentional Asymmetrical Electrodes. *ACS Appl. Electron. Mater.* **2020**, *2*, 769−779.
(53) Kim, J.; Ampadu, E. K.; Choi, W. J.; Oh, E. Photocurrent spectra from PbS photovoltaic infrared detectors using silver nanowires as plasmonic nano antenna electrodes. *Nanotechnology* **2019**, *30*, 075201.
(54) Jayawardena, K. D. G. I.; Thirimanne, H. M.; Tedde, S. F.; Huerdler, J. E.; Parnell, A. J.; Bandara, R. M. I.; Mills, C. A.; Silva, S. R. P. Millimeter-Scale Unipolar Transport in High Sensitivity Organic-Inorganic Semiconductor X-ray Detectors. *ACS Nano* **2019**, *13*, 6973−6981.
(55) Slonopas, A.; Alijabbari, N.; Saltonstall, C.; Globus, T.; Norris, P. Chemically deposited nanocrystalline lead sulfide thin films with tunable properties for use in photovoltaics. *Electrochim. Acta* **2015**, *151*, 140−149.
(56) An, Y. H.; Zhi, Y. S.; Cui, W.; Zhao, X. L.; Wu, Z. P.; Guo, D. Y.; Li, P. G.; Tang, W. H. Thickness Tuning Photoelectric Properties of β-Ga_2O_3 Thin Film Based Photodetectors. *J. Nanosci. Nanotechnol.* **2017**, *17*, 9091−9094.
(57) Yang, W.-H.; Jiang, X.-Y.; Xiao, Y.-T.; Fu, C.; Wan, J.-K.; Yin, X.; Tong, X.-W.; Wu, D.; Chen, L.-M.; Luo, L.-B. Detection of wavelength in the range from ultraviolet to near infrared light using two parallel $PtSe_2$/thin Si Schottky junctions. *Mater. Horiz.* **2021**, *8*, 1976−1984.
(58) Luo, L.-B.; Fang, T.; Xie, C.; Wang, L.; Wu, D.; Liang, F.-X. Distinguishing wavelength using two parallelly stacking graphene/thin Si/graphene heterojunctions. *J. Mater. Chem. C* **2021**, *9*, 8855−8861.

https://doi.org/10.1021/acsanm.2c01059
ACS Appl. Nano Mater. 2022, 5, 8894−8901